Electromagnetic Characterisation of a Short-Stroke Ferromagnetic Actuator

R. M. Inston and H. Karimjee

I. NOMENCLATURE

R_w, Winding resistance, $[\Omega]$

l_w, Length into the page of winding, [m]

A_w, Area of winding, $[m^2]$

V_w, Volume of winding, $[m^3]$

N, Number of turns in the winding, [-]

σ, Conductivity of winding, $[Sm^{-1}]$

k_{PF}, Packing factor of conductors in the winding, [-]

L, Inductance of the winding, [H]

$\mathcal{R}$, Reluctance, $[H^{-1}]$

A_{eff}, Effective area of air gap, $[m^2]$

W, Width of air gap, [m]

T, Thickness of air gap, [m]

g, Air gap length, [m]

II. INTRODUCTION

Finite Element Method Magnetics (FEMM) is an implementation of Finite Element Analysis (FEA) that specialises in electro-magnetics. This tool, in combination with MATLAB or another scripting language such as Python, can be used to create a series of numerical simulations, from which a electro-magnetic and then mechanical analysis can be extracted.

Here, FEMM is being used to characterise a magnetic actuator, outlined in [1], made up of an armature and a core which share the same ferromagnetic properties, two sets of windings around the top and bottom of the core and three air gaps of note, as in Fig 1. This characterisation will be done in four situations: analytically, neglecting and accounting for fringing, and numerically, using both a linear and non-linear ferromagnetic material.

III. MODEL MESHING

To perform FEA, a model is split into elements. The elements must be small enough to output an accurate enough answer despite the linearisation of the physics involved, whilst not being too small so as to increase the computational time to an unreasonable length.

FEMM has a smart-meshing tool in which the software analyses the model and allocates a dense mesh where higher resolution analysis is required and a sparse mesh where it is not. This is evident in the difference between figures 2 & 3. Although useful, this feature increases the mesh elements (see table I) without knowing any information about the overarching aim of the problem. This is illustrated at the boundaries of the variable air gap between the movable
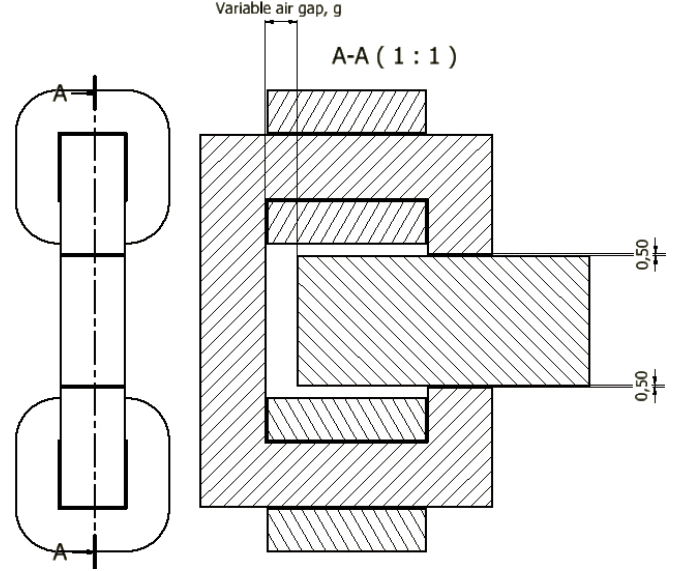

Fig. 1. Cross-sectional view of the actuator with the three air gaps higlighted (All measurements in mm).

armature and core, which is vital for the analysis of the force-displacement characteristic of the actuator. Smart-meshing fails to recognise these edges as paramount to the analysis and produces a grid seen in Fig 4. By manually setting the spacing of meshing along these lines as suggested in [2] Section II, FEMM can produce a denser, more regular mesh as seen in Fig 5. This accuracy has its cost in terms of mesh elements (Table I) and computational time; in running larger simulations than the ones carried out here, careful thought should be put into which areas of a model require more accurate analysis to avoid excessive computational requirements but maintaining a valid output.

Smart-meshing	Dense Air gap	Mesh Elements
OFF	OFF	14790
OFF	ON	16334
ON	OFF	22668
ON	ON	24368

TABLE I
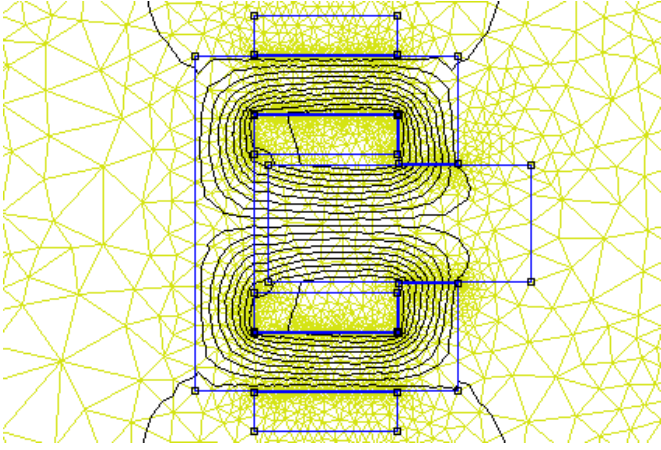A SUMMARY OF MESHING OPTIONS FOR THE MODEL.

Fig. 2. Example mesh with smart-meshing disabled. Note the sparseness of the triangulation.
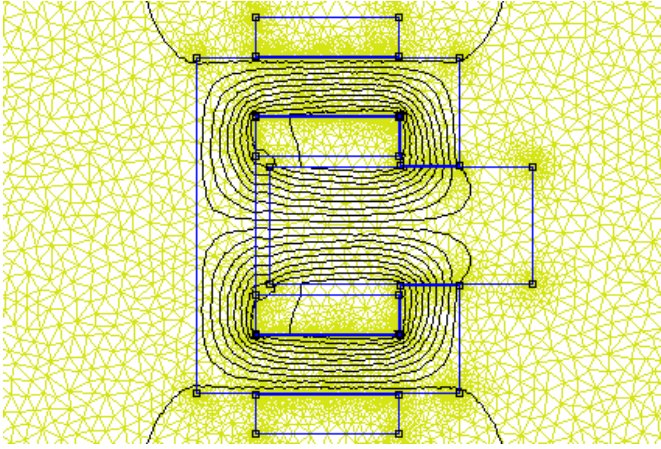

Fig. 3. Example mesh with smart meshing enabled. Note how the density increases around boundaries of interest.

IV. WINDING RESISTANCE

To calculate the winding resistance, R_w, two approaches were used: extracting resistance from FEMM and analytical. FEMM can calculate the winding resistance by obtaining the voltage and current across and through the winding respectively, and finding the resistance using Ohm's law. The analytical approach used block integrals in FEMM to obtain winding area and volume, and hence the winding depth (into the page) can be found using Eq 1:

$$l_w = \frac{V_w}{A_w} \qquad (1)$$

The analytical resistance is thus calculated using Eq 2. The resistances of each calculation method are presented in table II.

$$R_w = \frac{N l_w}{\sigma \left(\frac{k_{PF} A_w}{N} \right)} \qquad (2)$$

Table II shows a significant difference in estimated values. The analytical value uses a packing factor, $k_{PF} = 0.6$, that compensates for the space used by the insulating material in
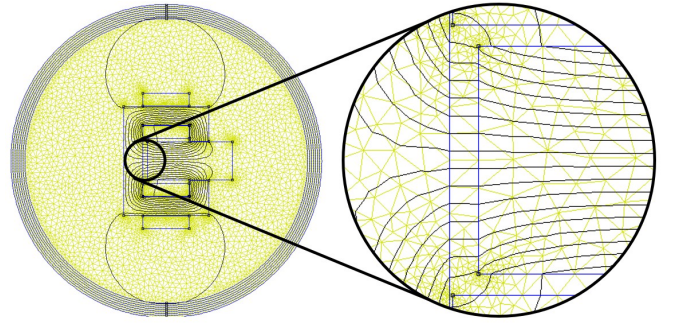

Fig. 4. FEMM smart-meshing output without specifying the area of interest. The density is low despite smart-meshing being on.
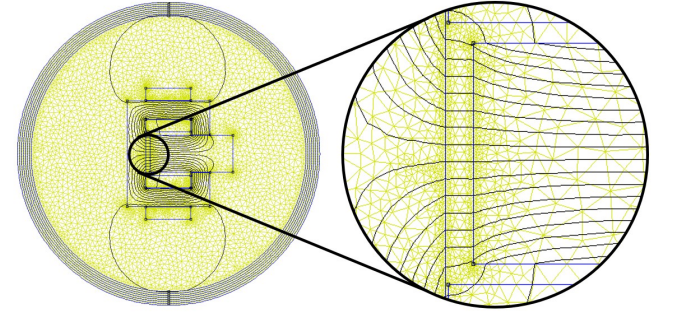

Fig. 5. FEMM smart-meshing output with specifying the area of interest and increasing the density of mesh elements within.

a winding. FEMM sees the entire area as conducting material and hence the implied cross sectional area of wire increases. Given the conductivity $\sigma = 58\text{MS/m}$ in both predictions, the greater the implied length of winding, the greater the winding resistance, R_w. However, FEMM is working with a 2D model and the analysis was performed on the top and bottom sections of the winding only. This means the analysis does not account for the whole length around the winding, notably the rounded corners and sides, causing the FEMM estimate to be at least a factor of four smaller than the analytical prediction.

Method	Current [A]	Winding Resistance [Ω]
FEMM	10	0.0107
Analytical	10	0.0557

TABLE II
A SUMMARY OF WINDING RESISTANCE CALCULATION FOR DIFFERENT METHODS.

The resistances resulting from these two methods were used to calculate the power loss through the windings for a range of current values using Eq 3. This was then plotted giving the graph in Fig 6. Clearly, this shows the power loss based on the analytically calculated resistance quickly becomes far greater than that of the FEMM calculated resistance. As such, if the analysis performed on the actuator were to be taken further into real applications, the analytical power loss should be considered when specifying power dissipation

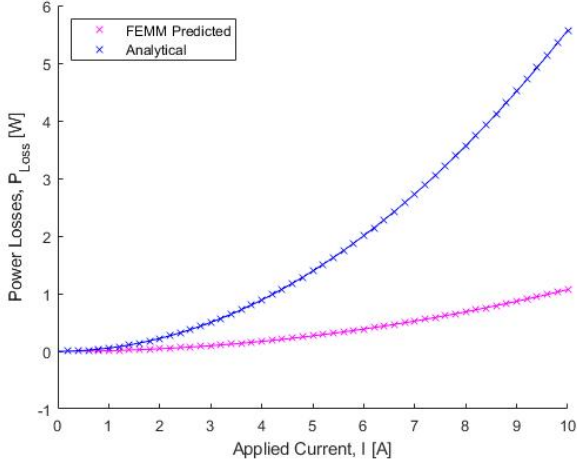requirements, rather than the FEMM output.

$$P_{loss} = I^2 R \tag{3}$$

Fig. 6. Power loss against current based on Eq 3 for analytical and FEMM calculated resistances. A quadratic curve produces the line of best fit.

V. WINDING INDUCTANCE

Similarly to the winding resistance, the inductance of the windings can be found analytically and numerically. The value can be calculated analytically with Eq 4.

$$L = \frac{N^2}{\sum \mathcal{R}} \tag{4}$$

Assuming flux is conserved, the total reluctance can be calculated based on a magnetic equivalent circuit, Fig 7. Note this is only half of the complete circuit for the actuator.

$$\sum \mathcal{R} = \mathcal{R}_{core} + \mathcal{R}_{air} + \mathcal{R}_{armature} + \mathcal{R}_{gap} \tag{5}$$

$$\mathcal{R} = \frac{l}{\mu_0 \mu_r A} \tag{6}$$

To improve accuracy, fringing effects can be taken into account by replacing A in Eq 6 with A_{eff} from Eq 7 for $\mathcal{R}_{airgap}$ and $\mathcal{R}_{variable}$.

$$A_{eff} = (W + 2g)(T + 2g) \tag{7}$$

As only half of the equivalent circuit (shown in Fig 7) was used to calculate the inductance, the result was doubled to obtain the effective inductance of the whole actuator. To allow for this, only half of the armature and variable air gap areas were used in the original calculation.

Assuming flux is conserved and then accounting for fringing gives two analytical values. Numerically, two values of inductance can be obtained from FEMM by using a linear and non-linear approximation of core and armature properties. FEMM outputs winding current and flux linkage
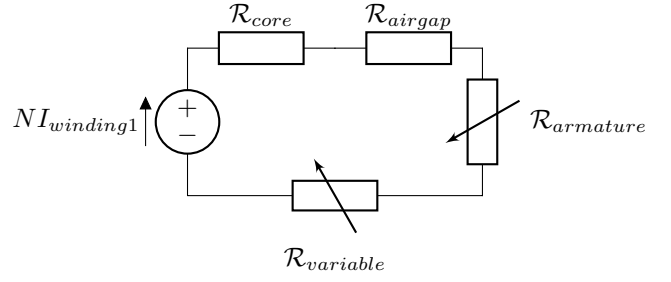

Fig. 7. Half equivalent magnetic circuit for the ferromagnetic actuator.

for each assigned internal circuit; from this inductance can be calculated with Eq 8. Winding current and flux linkage were obtained for one of the winding circuits, and an inductance calculated. As with the analytical inductance, this was then doubled to obtain the effective total inductance for both windings - only possible as the actuator is symmetrical.

$$L = \frac{\psi}{I} \tag{8}$$

The variation in inductance with armature displacement is shown in Fig 8. Clearly, the closer the armature is to the core the greater the inductance. This is the expected behaviour, as from Eq 4 a smaller total reluctance will give a larger inductance. The total reluctance is very sensitive to the width of the variable airgap and therefore the armature position. As air has a much smaller relative permeability (μ_r) than the core material, a large airgap will dominate the circuit and give a large total reluctance which significantly limits the flux travelling around the circuit, giving a small inductance. As the airgap gets smaller, its reluctance drops and the core material begins to dominate the circuit with its higher relative permeability, leading to a lower total reluctance allowing more flux to travel arond the circuit, giving a higher inductance. The inductance for the non-linear core material shows the effect of saturation: as the armature approaches the closed position (-4.9mm displacement) the inductance doesn't follow the same trend as the numerically simulated linear material and analytical approaches.

The analytical model accounting for fringing effects has higher inductance at all actuator positions than the model assuming flux is conserved. This is due to fringing increasing the effective area of the airgap and therefore decreasing its reluctance.

For armature positions close to the core, the analytically calculated (with fringing) and numerically simulated inductances are very similar, which suggests the approximation of fringing effects using Eq 7 is relatively accurate for small airgap sizes. As the airgap increases however, the two inductances diverge significantly, suggesting the approximation is only accurate for small values of g.

VI. FORCE ON THE ARMATURE

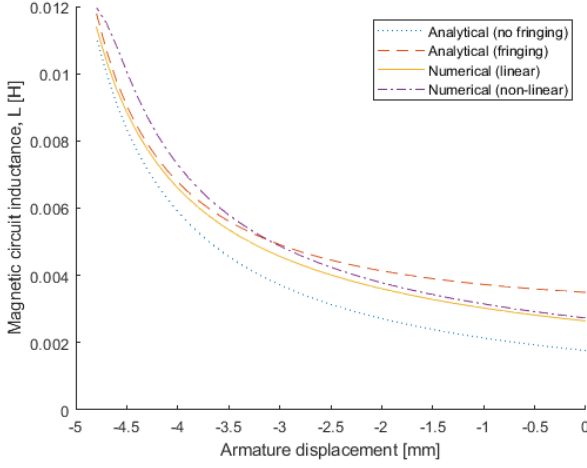The method for calculating the force on the armature is outlined in [2] Section VI. In following this method,

Fig. 8. Graph showing inductance versus armature displacement for the varying methods of calculation. Armature in open positon has zero displacement.

$\Psi - I$ diagrams were plotted with Ψ extracted from FEMM. The change in co-energy between armature positions was found by numerically integrating the area between curves (successive armature positions) in Fig 9. The force on the armature between each position was then calculated as in Eq 9, effectively taking work done and dividing it by displacement. This was done for 50 armature positions to maximise resolution without excessive computational time.

The $\Psi - I$ diagrams for the analytical and numerical linear situations follow the same pattern: Ψ linearly increasing with I, with a steeper gradient the closer the armature is to the core. This is sensible as the flux able to be pushed around the circuit by the magneto-motive force set up by the windings will increase both as the MMF is increased and as the reluctance of the magnetic circuit decreases. The numerical non-linear case is the most interesting, showing evidence of saturation when the actuator approaches the closed position where the curve begins to tail off. The analytical case with no fringing has the least flux linkage across armature positions as it has the highest reluctance flux path; the one accounting for fringing the highest flux linkage having the lowest reluctance flux path due to the increased airgap area.

$$F = \frac{\Delta E_{mech}}{\Delta x} \quad (9)$$

The four force-displacement graphs shown in Fig 10 have broadly similar characteristics, following an exponential trend where force increases as the armature approaches the closed position. The analytical cases show a higher force in closed position, and lower force in the open position than the linear numerical case, further suggesting that the fringing approximation is imperfect. The non-linear numerical case has the highest force through all armature positions until saturation begins to have an effect, which compared to the linear numerical case suggests the model is non-linear across the whole B-H curve rather than just accounting for

saturation.

From Fig 11 and Table III, the force and co-energy calculated using the plotted $\Psi - I$ curves and those taken from FEMM are almost identical, with values only slightly different at a few displacements. This could be down to small errors in the numerical integration performed on the $\Psi - I$ curves. That these two curves match also suggests the analysis performed on the data extracted from FEMM in the other cases is also correct, as it followed the same methodology as for the non-linear case here.
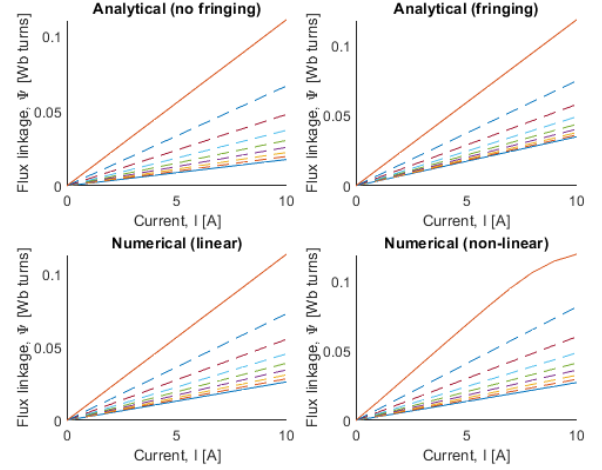

Fig. 9. Ψ-I diagrams for the four methods of calculating inductance. Note saturation reached in the non-linear graph. Shown for zero displacement, maximum displacement (-49mm) and seven linearly spaced intervals between (dashed lines).
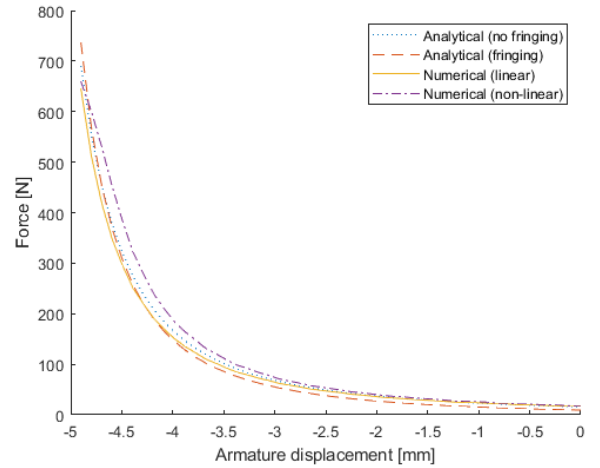

Fig. 10. Force versus displacement for the four methods of calculating inductance. Armature in open position at 0mm.

VII. Conclusion

References

[1] N. Simpson, *Electromagnetic characterisation of a short-stroke ferromagnetic actuator: Part a*, 2020.
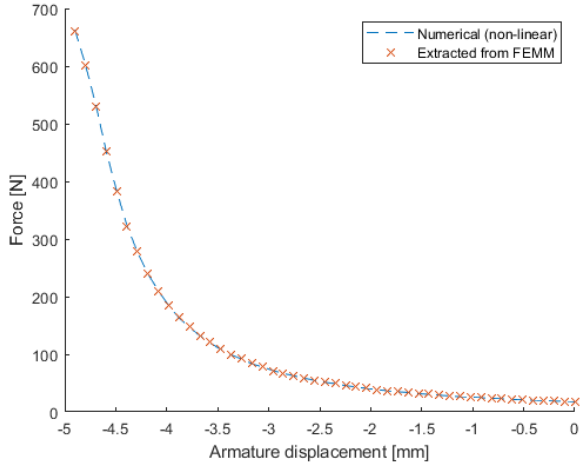
Fig. 11. Force versus displacement for the numerical non-linear case and extracted directly from FEMM.

[2] ——, *Electromagnetic characterisation of a short-stroke ferromagnetic actuator: Part b*, 2020.

Displacement [mm]	$\Delta E_{c_{(\Psi-I)}}$	$\Delta E_{c_{FEMM}}$
-0.1	0.0018	0.0018
-0.2	0.0018	0.0018
-0.3	0.0019	0.0019
-0.4	0.0020	0.0020
-0.5	0.0020	0.0020
-0.6	0.0021	0.0021
-0.7	0.0022	0.0022
-0.8	0.0023	0.0022
-0.9	0.0023	0.0024
-1.0	0.0025	0.0025
-1.1	0.0026	0.0026
-1.2	0.0026	0.0026
-1.3	0.0027	0.0028
-1.4	0.0029	0.0028
-1.5	0.0031	0.0031
-1.6	0.0032	0.0032
-1.7	0.0033	0.0033
-1.8	0.0035	0.0035
-1.9	0.0037	0.0037
-2.0	0.0038	0.0039
-2.1	0.0041	0.0040
-2.2	0.0044	0.0044
-2.3	0.0045	0.0045
-2.4	0.0049	0.0049
-2.5	0.0052	0.0051
-2.6	0.0055	0.0055
-2.7	0.0058	0.0059
-2.8	0.0062	0.0062
-2.9	0.0067	0.0067
-3.0	0.0071	0.0072
-3.1	0.0079	0.0078
-3.2	0.0084	0.0083
-3.3	0.0092	0.0092
-3.4	0.0098	0.0099
-3.5	0.0108	0.0109
-3.6	0.0121	0.0119
-3.7	0.0131	0.0132
-3.8	0.0148	0.0147
-3.9	0.0164	0.0163
-4.0	0.0183	0.0185
-4.1	0.0210	0.0210
-4.2	0.0239	0.0240
-4.3	0.0279	0.0277
-4.4	0.0322	0.0323
-4.5	0.0383	0.0383
-4.6	0.0452	0.0453
-4.7	0.0529	0.0533
-4.8	0.0601	0.0602
-4.9	0.0659	0.0663

TABLE III
TABULATED DATA FOR THE CHANGE IN CO-ENERGY BETWEEN EACH SIMULATED POSITION. CHANGE GIVEN BETWEEN TABULATED AND PREVIOUS DISPLACEMENTS.